PNAS RESEARCH ARTICLE | PHARMACOLOGY OPEN ACCESS

A structural mechanism of nuclear receptor biased agonism

Michelle D. Nemetchek[a,b,1], Ian M. Chrisman[a,b,1], Mariah L. Rayl[a,b], Andrew H. Voss[c], and Travis S. Hughes[a,b,c,2]

Edited by Steven Kliewer, The University of Texas Southwestern Medical Center, Dallas, TX; received September 7, 2022; accepted October 31, 2022

Efforts to decrease the adverse effects of nuclear receptor (NR) drugs have yielded experimental agonists that produce better outcomes in mice. Some of these agonists have been shown to cause different, not just less intense, on-target transcriptomic effects; however, a structural explanation for such agonist-specific effects remains unknown. Here, we show that partial agonists of the NR peroxisome proliferator-associated receptor γ (PPARγ), which induce better outcomes in mice compared to clinically utilized type II diabetes PPARγ-binding drugs thiazolidinediones (TZDs), also favor a different group of coactivator peptides than the TZDs. We find that PPARγ full agonists can also be biased relative to each other in terms of coactivator peptide binding. We find differences in coactivator–PPARγ bonding between the coactivator subgroups which allow agonists to favor one group of coactivator peptides over another, including differential bonding to a C-terminal residue of helix 4. Analysis of all available NR–coactivator structures indicates that such differential helix 4 bonding persists across other NR–coactivator complexes, providing a general structural mechanism of biased agonism for many NRs. Further work will be necessary to determine if such bias translates into altered coactivator occupancy and physiology in cells.

nuclear receptor | biased agonism | functional selectivity | selective modulator | fluorescence anisotropy

Significance

The potential of biased nuclear receptor agonists to provide superior therapeutic outcomes compared to clinically important drugs has generated long-standing interest in their development. A well-supported mechanism by which biased agonists could create improved outcomes is by causing the receptor to favor different coactivators than a reference drug. Despite the potential utility of biased agonists, a structural explanation of biased agonism is lacking. Here, we reveal differences in how coactivators bind nuclear receptors that allow several agonists to favor a different group of coactivator peptides than clinically used drugs. While further work is necessary to determine if similar coactivator preference occurs in cells, this structural explanation provides a foundation for rational development of nuclear receptor agonists which favor select coactivators.

One in six FDA-approved drugs targets a nuclear receptor (NR) (1), and many of these drugs offer unique clinical benefits. For example, thiazolidinediones (TZDs) treat diabetes by binding to the NR peroxisome proliferator-associated receptor γ (PPARγ), restoring insulin sensitivity and controlling blood glucose better than first-line type II diabetes treatments (2). However, TZDs also cause plasma volume expansion, weight gain, and increased bone fracture risk (3), limiting their use.

Some experimental agonists provide potentially superior therapeutic effects compared to clinically used NR binding drugs (4, 5). For example, when compared to TZDs in rodents, some PPARγ partial agonists cause fewer adverse effects but equivalent beneficial effects by selective activation of a subset of all PPARγ target genes (4). While some of these experimental agonists made it to clinical trials, none have been approved for human use. Despite their potential utility, we don't understand the mechanisms by which some NR agonists produce distinct, not just more or less intense, physiologic effects compared to reference agonists.

We know that NRs are ligand-responsive transcription factors that bind to genomic enhancers and modulate the transcription of associated genes. Agonist binding recruits coactivators to the receptor, increasing gene expression. A common current model of NR structure–function posits that different agonists drive the recruitment of a similar mix of coactivators to the receptor, activating target genes. An underlying assumption of this model is that the relative affinities of all coactivators are maintained for all NR–agonist complexes; however, many reports raise the possibility that some agonists skew, or bias, coactivator recruitment relative to other agonists (4). Coactivator bias, coupled with the unique, and possibly context-dependent effects of individual coactivators (6–8) could cause the distinct transcriptomic and physiologic effects observed for different agonists (4). Coactivator bias could also affect posttranslational modification of PPARγ (9), as coregulator association may lead to PPARγ post-translational modification (10). Despite the potential therapeutic benefits of ligand-tunable coactivator bias, the structural mechanisms of coactivator bias remain unknown. Furthermore, a shortcoming of previous reports of coactivator bias is that bias was not quantified but implied from binding data, preventing statistical testing of the phenomena and comparison of bias between agonists.

Here, we precisely measure coactivator bias induced by a handful of ligands by measuring the affinity of the full-length PPARγ signaling complex for LxxLL motif-containing regions of coactivators (where x is any amino acid and L is leucine), which we refer to as coactivator peptides. The LxxLL forms a two-turn helix, surrounded by apparently unstructured regions as judged by structures predicted by Alphafold (11), and existing NR–coactivator structures (12). Such regions are known to drive the binding of the coactivator

Author contributions: M.D.N., I.M.C., M.L.R., and T.S.H. designed research; M.D.N., I.M.C., M.L.R., and A.H.V. performed research; M.D.N., I.M.C., M.L.R., and T.S.H. analyzed data; and M.D.N., I.M.C., M.L.R., and T.S.H. wrote the paper.

The authors declare no competing interest.

This article is a PNAS Direct Submission.

[1]M.D.N. and I.M.C. contributed equally to this work.

[2]To whom correspondence may be addressed. Email: travis.hughes@umontana.edu.

This article contains supporting information online at https://www.pnas.org/lookup/suppl/doi:10.1073/pnas.2215333119/-/DCSupplemental.

Published December 5, 2022.

to NRs (13–16). We find that a full agonist and several partial PPARγ agonists create coactivator peptide bias relative to TZDs. Precise quantification of coactivator bias coupled with analysis of new and existing PPARγ structures reveals coactivator–receptor interactions that allow coactivator bias in PPARγ. One key bias-relevant interaction is the bonding between coactivators and a C-terminal residue on PPARγ helix 4. The presence of this bond makes the coactivator affinity more dependent on the structural state of the C-terminal helix of the receptor, helix 12 as compared to coactivator peptides that naturally lack this bond. Agonists which do not stabilize helix 12 well, such as PPARγ partial agonists, favor coactivators that lack this bond. In contrast, agonists that efficaciously stabilize helix 12, such as TZDs, favor peptides that make the bond. Analysis of all available NR–LxxLL structures suggests that differential helix 4 bonding and other mechanisms of coactivator bias revealed by this work likely allow biased agonism in other NRs.

Results

Full, Partial, and Nonagonists Are Biased Agonists Relative to a TZD. NR ligands which produce maximal, some, no, or decreased activity in a cell-based reporter assay are commonly referred to as full, partial, non, and inverse agonists, respectively (17–19). PPARγ partial agonists may induce distinct coregulator binding profiles from the prototypical full agonist, rosiglitazone (*SI Appendix*, Table S1). Most commonly, partial agonists appear to favor binding the metabolism-associated coactivator PGC1α (PPARγ coactivator 1α) over coactivators more directly associated with the core transcriptional machinery such as CBP [CREB binding protein (20, 21)] and MED1 (Mediator Complex Subunit 1) (22, 23).

Based on these reports, we hypothesized that two high-affinity partial agonists which induce less overall and heart weight gain compared to rosiglitazone in mice [MRL24 (24) and nTZDpa (25)] would also induce coactivator bias relative to rosiglitazone. In addition, we tested copurified *Escherichia coli* lipids for bias relative to rosiglitazone (26–28). Copurified *E. coli* lipids can act as partial agonists and may include endogenous PPARγ ligands (26). *E. coli* lipids are likely displaced by or cobind with the higher affinity synthetic ligands we use (*SI Appendix*, Table S2) (26, 29). We also tested the coregulator binding profile of the delipidated (apo) ligand binding domain (LBD) of PPARγ (see below).

To determine how the partial agonists affect PPARγ's coregulator binding profile, we measured dissociation constants (K_d) for the binding of PPARγ-partial agonist complexes to fluorescein-tagged coactivator peptides ($PGC1\alpha_{144}$ or CBP_{70}) using fluorescence anisotropy. We denote coregulator peptides by the coregulator name followed by the number of the first leucine in the LxxLL (30) or corepressor (LxxI/VIxxxF/Y/L) (31) motif contained in the peptide (e.g., CBP_{70} contains the LxxLL motif at residues 70 to 74). To obtain K_d values, we measure coregulator anisotropy for three PPARγ-containing complexes: the PPARγ–ligand complex, the PPARγ–ligand complex heterodimerized to retinoid X receptor α (RXRα), and the heterodimer bound to DNA (32) (Fig. 1*A*).

We found that rosiglitazone, both partial agonists (i.e., nTZDpa and MRL24), and copurified *E. coli* lipids induce similar heterodimer affinity for one LxxLL motif peptide [$PGC1\alpha_{144}$ (33)]; however, rosiglitazone induces higher affinity for another LxxLL motif peptide [CBP_{70} (21); Fig. 1*B*]. These data suggest that the different physiologic effects of rosiglitazone and the partial agonists (25, 34) could arise from differential coactivator recruitment. We also found that off-target binding to other PPAR family members is unlikely to explain the previously reported different physiologic outcomes of nTZDpa, MRL24, and rosiglitazone as all three ligands have at least 3,000-fold lower affinity for PPARδ and PPARα than for PPARγ (*SI Appendix*, Table S2). We also tested the coregulator binding profile of a non-TZD full agonist [GW1929 (35)], which, like rosiglitazone, induces maximal transcription from a reporter plasmid (*SI Appendix*, Fig. S2). Like the partial agonists, GW1929 also generates a distinct coactivator peptide binding profile from rosiglitazone, inducing higher affinity for $PGC1\alpha_{144}$ but not CBP_{70} (Fig. 1*C*).

Coactivator preference has been primarily reported qualitatively, making it difficult to compare preference across ligands or reports. To overcome this limitation, we calculated ligand benchmark bias (36, 37) from our measured K_d values. We use the TZD rosiglitazone as the reference ligand in these calculations because we want to determine whether non-TZD ligands create different coregulator binding profiles from rosiglitazone. We chose to use the affinity of CBP_{70} for PPARγ as the reference signal (37), which sets the average CBP_{70} bias value to zero (Fig. 1*F*). Using this method, we consider an agonist that generates significantly nonzero bias values for at least one other coactivator peptide as biased relative to rosiglitazone.

Our bias calculations reveal positive bias values for the non-TZD ligands GW1929, MRL24, and nTZDpa for $PGC1\alpha_{144}$ relative to rosiglitazone (Fig. 1 *D* and *E*). We performed a similar experiment with the addition of LxxLL-containing peptides from MED1 ($MED1_{645}$), the context-dependent coregulator (6) NR interacting protein-1 (38) ($NRIP1_{501}$), and an IxxIIxxxF CoRNR (31) peptide from NR corepressor 1 (39) ($NCOR1_{2263}$). This follow-up experiment showed that the non-TZD ligands favor LxxLL peptides from both $NRIP1_{501}$ and $PGC1\alpha_{144}$ relative to $MED1_{645}$ and CBP_{70} and that just the partial agonists (MRL24 and nTZDpa) favor the corepressor peptide $NCOR1_{2263}$ (Fig. 1*G*). We also confirmed that bias in the heterodimer is driven by PPARγ, not RXRα (*SI Appendix*, Fig. S1). To illustrate the possible impact of such bias values on the coactivator binding profile, we calculated hypothetical PPARγ occupancy using K_d values underlying Fig. 1*G* assuming excess coactivator peptide. This calculation indicates that GW1929 and the partial agonists would tilt PPARγ occupancy toward PGC1α (Fig. 1*H*).

These ligands induced favorable binding of some LxxLL-containing peptides relative to others, yielding bias values between 0.2 and 0.4. To put these values in perspective, we calculated bias produced by the inverse agonist, T0070907 (18), for a corepressor peptide ($NCOR1_{2263}$) relative to the agonist rosiglitazone. T0070907 produces opposite effects from rosiglitazone on gene expression (40) (*SI Appendix*, Fig. S2) and coregulator affinity (18). As expected, T0070907 strongly favors $NCOR1_{2263}$ binding relative to rosiglitazone, producing bias values between 1 and 1.5, which are likely near the maximum possible for PPARγ (*SI Appendix*, Fig. S2). We also measured bias for two nonagonists/antagonists, a partial agonist and two additional TZDs (pioglitazone and troglitazone). Like the partial agonists tested above, most of the non-TZD antagonists and partial agonists appear to favor select coactivator peptides and the corepressor peptide (i.e., $PGC1\alpha_{144}$ and $NCOR1_{2263}$). The two TZDs (pioglitazone and troglitazone) produce near zero bias values for all peptides except the corepressor ($NCOR1_{2263}$); however, these TZDs have much lower affinity for PPARγ compared to the other ligands we used, leaving PPARγ partially ligand-free near the dissociation constant of the peptides (*SI Appendix*, Fig. S2).

The coactivator peptide bias we observe is not significantly affected by the fluorescent label. Unlabeled, N, and C terminally labeled

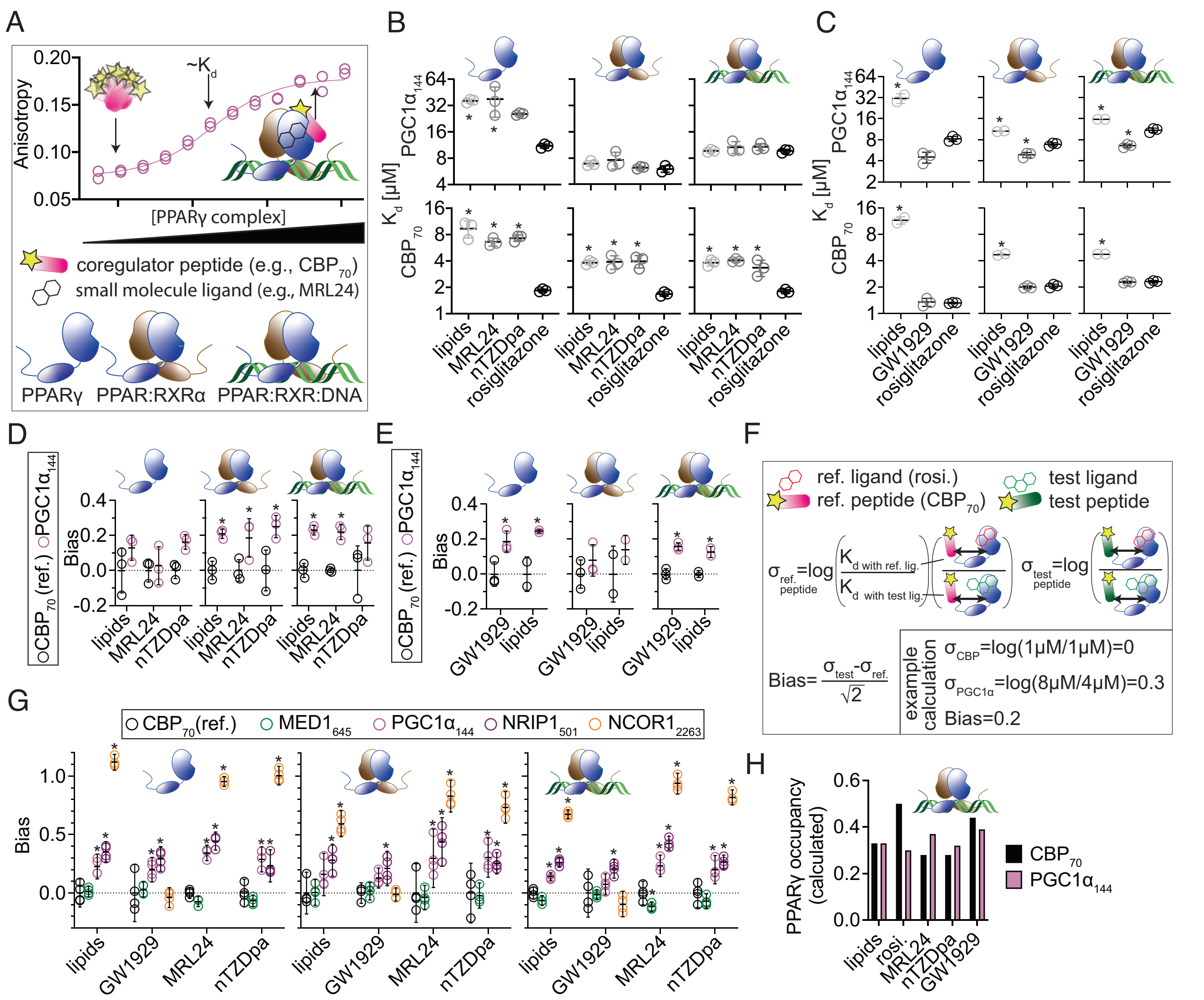

Fig. 1. Two partial agonists and a full agonist are biased agonists relative to rosiglitazone. (*A*) Fluorescence anisotropy assay method. (*B* and *C*) Dissociation constants (K_d) of the indicated PPARγ–ligand signaling complexes for fluorescein-labeled CBP_{70} or $PGC1\alpha_{144}$ coregulator peptides are displayed (n = 3 except for lipids in panel *C* where n = 2). Lipids refers to copurified *E. coli* lipids. *Adjusted $P < 0.05$ compared to rosiglitazone. Each circle represents affinity measurements using an independent serial dilution of PPARγ from the same purification batch. (*D* and *E*) Bias values were calculated from K_d values shown in panels *B* and *C*. *Adjusted $P < 0.05$ compared to CBP_{70}. (*F*) Bias value calculation method. (*G*) Bias values for additional coactivator peptides and a corepressor peptide (n = 4). *Adjusted $P < 0.05$ compared to CBP_{70}. (*H*) Fraction of PPARγ occupied by CBP_{70} and $PGC1\alpha_{144}$ under competitive binding calculated using K_d values underlying data in panel *G* for the DNA-bound heterodimer. See *Methods* for calculation assumptions. Mean and SD are displayed. All data analyzed using one- or two-way ANOVA followed by Dunnett's or Sidak's multiple comparisons test. The data points and raw data underlying these graphs are found in Datasets S1 and S2, respectively. See Dataset S3 for additional statistical details.

peptides produce similar bias values (*SI Appendix*, Fig. S3). In addition, isothermal titration calorimetry (ITC) experiments using unlabeled peptides confirmed that CBP_{70} and $MED1_{645}$ bind to rosiglitazone and GW1929–receptor complexes with similar affinity (*SI Appendix*, Fig. S3). ITC of $NRIP1_{501}$ and $PGC1\alpha_{144}$ binding to PPARγ produced little to no detectable heat, preventing bias calculation for these peptides. Despite this, their distinct thermodynamic binding signatures suggest that they bind differently to PPARγ.

Differential Bonding to Helix 4 Allows LxxLL Bias. Because LxxLL peptides have very similar binding modes, it is not apparent how these ligands could favor certain LxxLL peptides over others. The coregulator binding site for almost all NRs consists of a hydrophobic groove bookended by a lysine and glutamate residue (termed the helix 3 and 12 charge clamps; $H3_{cc}$ and $H12_{cc}$). The amphipathic coactivator LxxLL helix slots into this hydrophobic groove and the ends of the helix bond to $H3_{cc}$ and $H12_{cc}$. We reasoned that additional less-appreciated interactions between the receptor LBD and LxxLL peptides underlie bias. We first confirmed that the PPARγ LBD is sufficient to produce bias (Fig. 2*A*). We used delipidated PPARγ for these and all other LBD experiments reported here, which also demonstrates that the presence of copurifying lipids is not necessary for bias.

To identify bias-relevant coactivator residues, we performed bias measurements using all 16 coactivator peptides with potentially high affinity for PPARγ from a published screen of ~150 coactivator peptides (41) and two nonnatural peptides (42). These data indicate that GW1929 and MRL24 bias PPARγ binding toward peptides with SxxLxxLL or S/TxLxxLL motifs (S and T signify serine or threonine) and away from those with a H/NxxLxxLL motif (Fig. 2*B*). Furthermore, the comparison of bias to affinity indicates that peptide affinity does not determine bias (Fig. 2*C*).

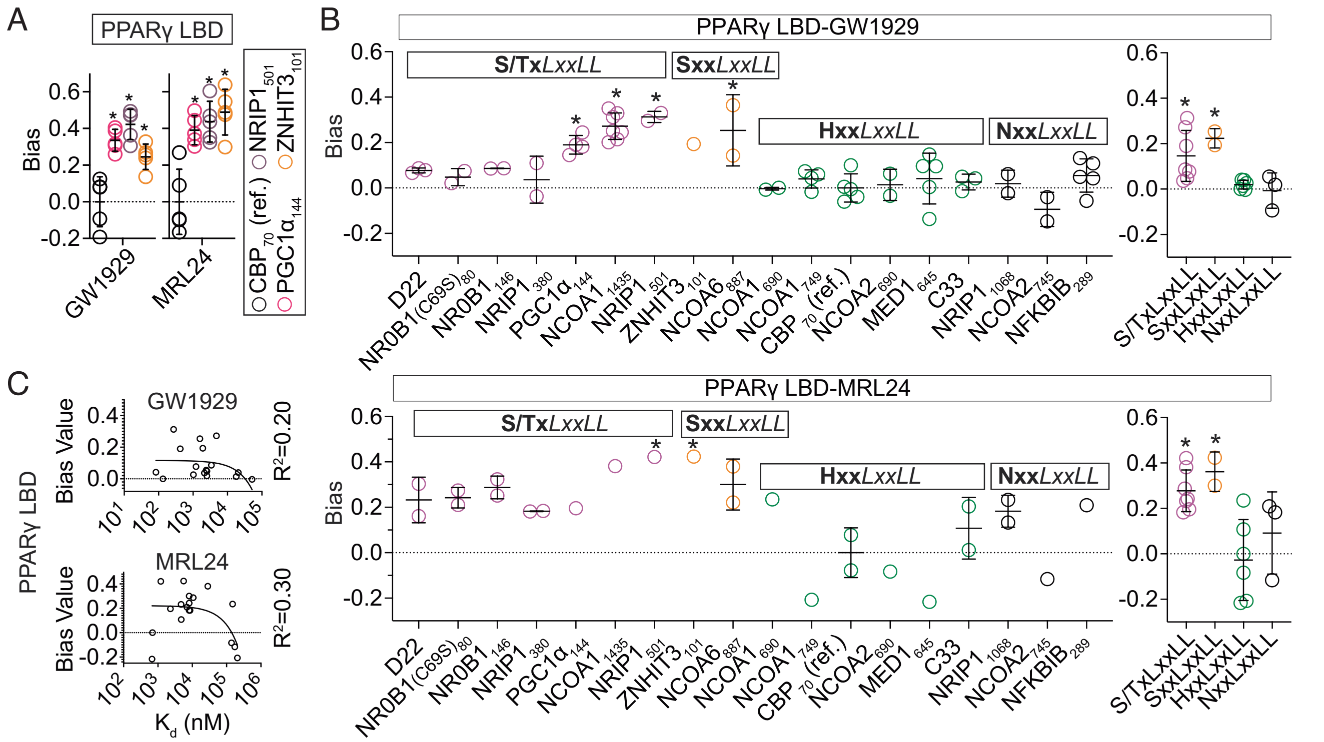

Fig. 2. Residues adjacent to the LxxLL motif correlate with bias. (*A*) Bias for the indicated complexes. *Adjusted $P < 0.05$ compared to CBP_{70}. Each circle represents an experiment using independent serial dilutions of the same PPARγ purification batch (n = 5). (*B*) Bias, derived from peptide–PPARγ dissociation constants. For each peptide, each circle represents an independent anisotropy experiment using PPARγ LBD from a separate purification batch, except for three data points for $NCOA1_{1435}$, which represent different serial PPARγ dilutions from the same batch. The average of the bias values shown in the *Left* panels were sorted by sequence motif and graphed in the *Right* panels. *Adjusted $P < 0.05$ compared to CBP_{70} (*Left*) or H motif coactivators (*Right*). Number of data points vary; see *SI Appendix* for details. Individual values, mean, and SD are displayed. Two of the listed peptides have an LxxML sequence (where M is methionine; $NRIP1_{1068}$ and $NR0B1_{80}$); however, for clarity, we use LxxLL to refer to all peptides. (*A* and *B*) Statistical analysis done using ANOVA followed by Dunnett's or Sidak's multiple comparisons test. (*C*) Poor correlation between K_d and bias values for data shown in panel *B*. Linear regression produced the displayed R^2 values. The data points and raw data underlying these graphs are found in Datasets S1 and S2, respectively. In addition, see Dataset S3 for statistical comparison and linear regression details.

To better understand the structural mechanisms of coactivator peptide bias, we solved the structures of the PPARγ LBD bound to the two H/NxxLxxLL peptides with the highest affinity for PPARγ ($MED1_{645}$ and CBP_{70}; Fig. 3*A* and *SI Appendix*, Table S3) and compared these structures to previously solved structures of PPARγ bound to S/TxLxxLL peptides with the highest affinity for PPARγ ($PGC1\alpha_{144}$ and $NCOA1_{1435}$). The HxxLxxLL motif-containing structures show the bonding between the H motif histidine and PPARγ helix 4 (K319) while S/TxLxxLL peptides do not bond to PPARγ helix 4 (Fig. 3*A*). Further analysis of all PPARγ–LxxLL motif structures shows that HxxLxxLL motif peptides either bond to K319 or possess a peptide N-terminus that is oriented toward helix 4 (Fig. 3*C* and *SI Appendix*, Fig. S6). The importance of peptide-K319 bonding is demonstrated by the fivefold loss in affinity and altered binding thermodynamics caused by its disruption in CBP_{70} (*SI Appendix*, Fig. S3).

Alignment of helix 4 residues in the 38 NRs that bind the LxxLL helix well (i.e., those where the $H12_{cc}$ and $H3_{cc}$ side chains are negative and positive, respectively) reveals that the residue analogous to K319, which we term $H4_8$, is always capable of hydrogen bonding (Fig. 3*D*). We identified nearly 700 structures containing 19 different LxxLL motifs bound to 29 of these 38 NRs. Analysis of hydrogen bonding between peptide and the receptor in these structures shows that the $H4_8$ bond is the only peptide–receptor bond that is prevalent in H/NxxLxxLL peptide-containing structures but not SxxLxxLL or S/TxLxxLL peptide structures (Fig. 3*E* and *SI Appendix*, Fig. S4). $H4_8$ bonds to the H or N of the H/NxxLxxLL motif, except in Estrogen Receptor α-$NCOA1_{690}$ and $NCOA2_{690}$ structures where $H4_8$ bonds with an adjacent lysine (HKxLxxLL). Comparison of these structural data and bias in PPARγ suggests that bonding between $H4_8$ and coactivator residues 2 or 3 residues N-terminal to the first leucine of the LxxLL helix coactivator is an important structural feature underlying coactivator bias for many NRs. We term coactivator peptides displaying this binding mode N-anchored peptides. Analysis of 40 additional structures containing nonnatural (43) and LxxLL-like motifs reveals two androgen receptor (AR) structures with bonding between the S of an SxxLxxLL motif and the AR $H4_8$ glutamine, indicating that the N-anchored binding mode can depend on the NR binding partner.

Natural SxxLxxLL and S/TxLxxLL motif peptides do not bond with $H4_8$ and behave similarly in terms of PPARγ bias, so we refer to such peptides here as S motif peptides. We tested the impact of N-anchored $H4_8$ bonding on bias using both direct and competitive anisotropy. Disruption of the $H4_8$ bond for CBP_{70} (CBP_{70}H67A) and $MED1_{645}$ ($MED1_{645}$H642A) decreases affinity and, as expected, increases bias for both PPARγ–GW1929 and PPARγ–MRL24 complexes (Fig. 4 *B* and *C* and *SI Appendix*, Fig. S4). These data indicate that the presence or absence of bonding to $H4_8$ contributes to coactivator bias.

We also tested the impact of S/T helix capping on bias. S/T capping occurs when the side chain of a serine or threonine near the helix N-terminus bonds to an exposed helix amine, stabilizing the helix (45, 46) (Fig. 3*A*) and occurs in the majority of PPARγ–S/TxLxxLL motif-containing structures but none of the PPARγ–SxxLxxLL or N-anchored structures (*SI Appendix*, Fig. S4). S/T capping has been shown to affect PGC1α function (47). When present, the S/T cap satisfies one otherwise exposed helix amine

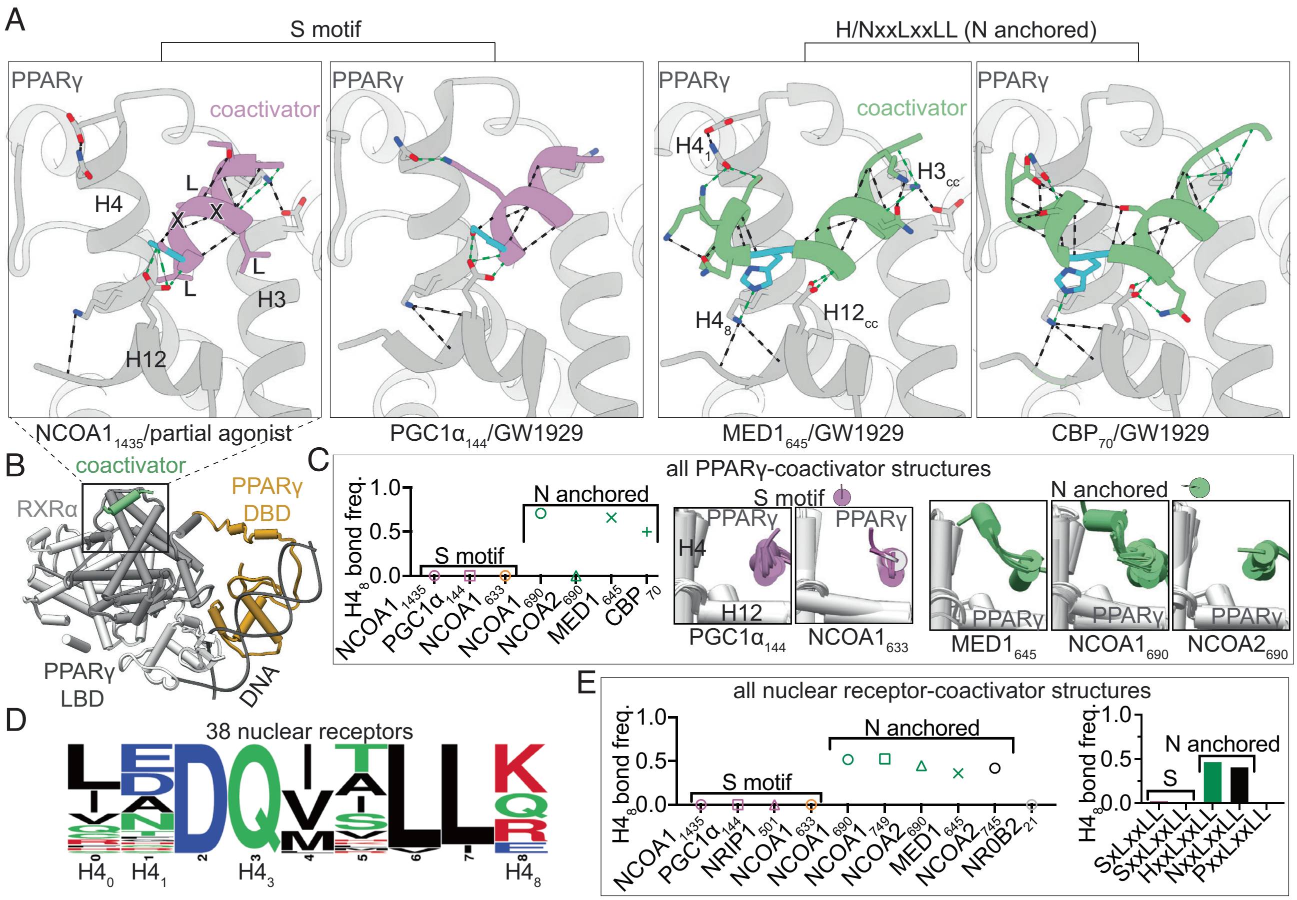

Fig. 3. Residues adjacent to the LxxLL motif determine helix 4 bonding. (*A*) Our structures of the PPARγ LBD bound to N-anchored peptides (CBP_{70} or $MED1_{645}$) and previously reported structures of the PPARγ LBD bound to S motif peptides ($PGC1\alpha_{144}$ or $NCOA1_{1435}$). Bonds involving a peptide are shown as dashed lines. The most N-terminal residue of the helix (N-cap residue) is shown in cyan. PDB codes 4Y29, 6FZP, 6D94, and 7RLE. For crystallography data and refinement statistics, see *SI Appendix*, Table S6. (*B*) An example PPARγ–RXRα heterodimer structure (PDB code 3DZY). DNA binding domain (DBD). (*C*) Aligned overlay of all available PPARγ–coactivator structures except three which are shown in *SI Appendix*, Fig. S6 for clarity. The drawings above the structures illustrate the angle in which the coactivator loop backbone enters the helix in almost all PPARγ structures containing such coactivators. (*D*) Conservation of helix 4 residues across all 38 NRs that likely bind well to an LxxLL helix. Four helix 4 residues that often bind to coactivators are indicated ($H4_0$, $H4_1$, $H4_3$, and $H4_8$). (*E*) Fraction of NR–coactivator structures with three or more available structures that have a coactivator–$H4_8$ hydrogen bond. The data points underlying these graphs are found in Dataset S1.

and shortens the LxxLL helix (relative to N-anchored peptides), pointing the N-terminal part of the peptide away from helix 4 (*SI Appendix*, Fig. S4). We found that disruption of the S/T cap affects peptide affinity and has a small effect on bias for just the PPARγ–GW1929 complex (Fig. 4*D*). Because the S142 side chain often bonds to $H12_{cc}$, in addition to capping the helix, these results are consistent with the idea that S/T capping, $H12_{cc}$ bonding, or both affect bias generated by GW1929.

We next investigated a peptide–receptor bond that is similar to N-anchored bonding but on the opposite (C-terminal) end of the LxxLL helix. This bond ($NRIP1_{501}$H507 to $H4_3$) is prevalent in $NRIP1_{501}$-RAR-related orphan receptor (ROR) structures (Fig. 4*A* and *SI Appendix*, Fig. S4). $NRIP1_{501}$ has a CCapG motif (45) that follows the LxxLL helix (i.e, LxxLLGH where G is glycine) which may allow the geometry necessary for the H507–$H4_3$ bond. While there are no available structures of $NRIP1_{501}$ bound to PPARγ, $H4_3$ is a glutamine in all 38 NRs we structurally analyzed above, including PPARγ, so it is likely that such a bond is also present in the PPARγ–$NRIP1_{501}$ complex. As anticipated, we found that mutation of $NRIP1_{501}$ H507 decreases affinity for WT PPARγ and various PPARγ mutants, indicating that PPARγ $H4_3$ also bonds with $NRIP1_{501}$ H507 (*SI Appendix*, Fig. S4). Furthermore, disruption of this bond decreases bias produced by GW1929, indicating that such C-terminal bonding can affect coactivator bias values compared to peptides that lack such bonding (Fig. 4*E*). Further supporting this idea, $NRIP1_{501}$ repeatedly yielded nominally higher bias values than $PGC1\alpha_{144}$, which lacks such bonding (Figs. 1*G* and 2 *A* and *B*).

Together, these mutational data indicate that differential bonding to helix 4 underlies coactivator peptide bias. In addition, the fact that some interactions are important for bias produced by MRL24 but are less important for GW1929 (and vice versa) indicates that these ligands achieve bias using different structural mechanisms.

N-Anchored Peptide Affinity Is More Sensitive to Helix 12 Structure. We investigated how differential $H4_8$ bonding yields bias. Because $H12_{cc}$ and $H4_8$ hydrogen bond with nearby residues on N-anchored peptides (Fig. 4*A*), we reasoned that $H12_{cc}$ disruption may also disrupt the $H4_8$ bonding of N-anchored peptides. Such $H12_{cc}$–$H4_8$ bond interdependence would make N-anchored peptides more sensitive to helix 12 structure than S motif peptides, which lack bonding to $H4_8$. In the absence of such bond interdependence, $H12_{cc}$ mutation should affect S motif and N-anchored coactivator peptides similarly because $H12_{cc}$ bonds similarly to the LxxLL helix backbone of all coactivators (Fig. 4*A*). Consistent with $H12_{cc}$–$H4_8$ bond interdependence, mutation of $H12_{cc}$ has an outsized impact on N-anchored peptide affinity.

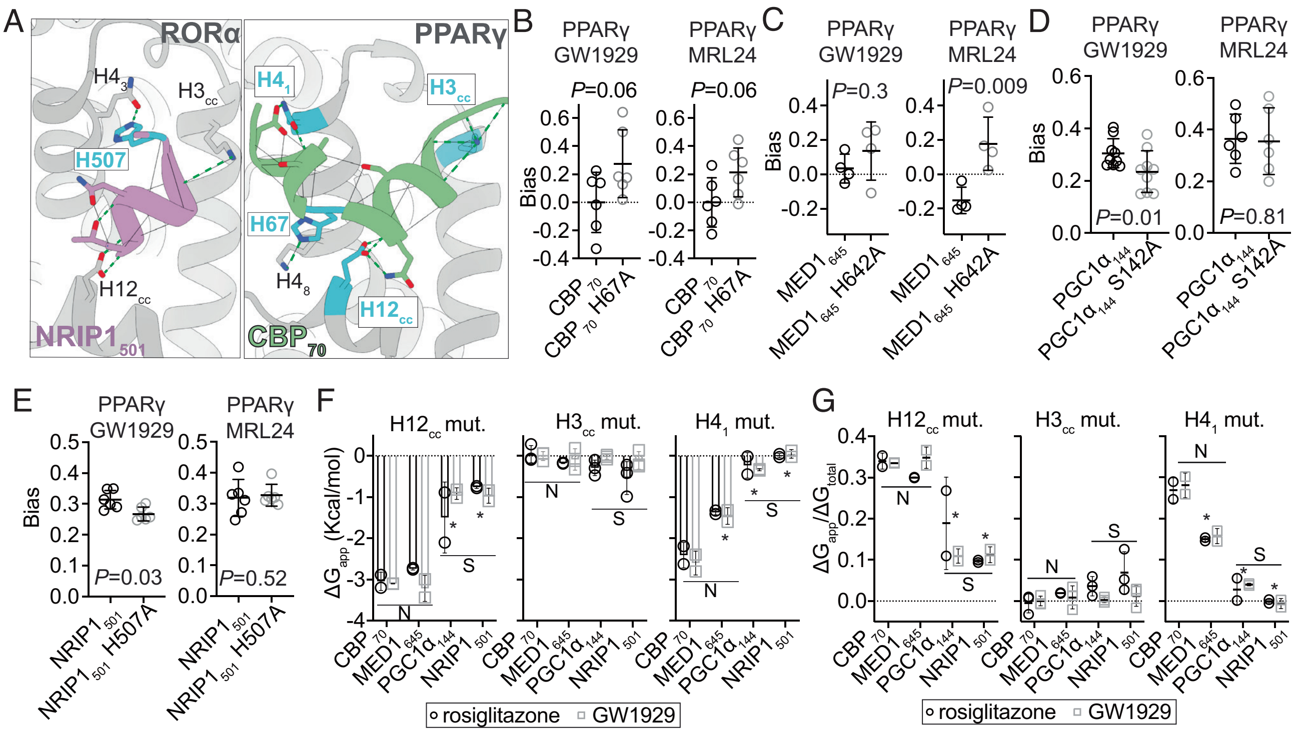

Fig. 4. Structural determinants of coactivator bias. (*A*) Residues mutated in panels *B*–*G* are colored cyan. Our CBP$_{70}$–PPARγ LBD structure and a previously published structure of ROR LBD bound to NRIP1$_{501}$ (44) (PDB codes 7RLE and 5NTW) are shown. Hydrogen bonds shown as dashed lines. (*B* and *C*) Mutation of the N-anchored bond increases bias values. (*B*) Competitive anisotropy was used to measure the impact of CBP$_{70}$H67–H4$_8$ bond disruption. (n = 6). (*C*) Direct anisotropy was used to measure impact of MED1$_{645}$ H642–H4$_8$ bond disruption (n = 4). (*D*) Disruption of the PGC1α$_{144}$ S/T cap affects bias for PPARγ LBD bound to GW1929 (n = 9) but not MRL24 (n = 6). Pooled data from three independent experiments. Some of the nonmutant data points are used in Fig. 2. Each circle represents an independent experiment using either an independent PPARγ serial dilution or PPARγ from different protein purifications. (*E*) NRIP1$_{501}$H507A mutation reduces GW1929, but not MRL24, bias (n = 6). (*B*–*E*) *P* values are from two-tailed t tests. (*B*, *C*, and *E*) Individual data points represent independent serial dilutions of PPARγ from stock. (*F*) Apparent bond energy (ΔG_{app}) of hydrogen bonds shown in panel *A* calculated by comparing dissociation constants of wild-type (WT) complexes with complexes containing PPARγ and peptide mutants that disrupt such bonds [PPARγE471L (H12$_{cc}$), PPARγK301A (H3$_{cc}$), and PPARγN312A (H4$_1$)]. Individual data points (n = 2) represent replicates using distinct protein purifications. H3$_{cc}$ data (n = 3) include an additional replicate from an independent experiment. (*G*) The fraction of the total binding energy contributed by ΔG_{app} from panel *F*. (*F* and *G*) *Adjusted *P* < 0.05 compared to CBP$_{70}$. Two-way ANOVA followed by Sidak's multiple comparisons test. (*B*–*G*) Individual values, mean, and standard deviation are displayed. All experiments displayed in this figure used the PPARγ LBD. The data points and raw data underlying these graphs are found in Datasets S1 and S2, respectively. In addition, see Dataset S3 for statistical comparison details.

Mutation of another helix 4 residue (H4$_1$) also has a larger impact on N-anchored peptide affinity compared to the S motif peptide PGC1α, which also bonds with H4$_1$ (Fig. 3*A*), suggesting that H4$_1$ disruption may also affect additional N-anchored peptide bonds. In contrast, H3$_{cc}$ mutation (PPARγ K301A) has a smaller, fairly uniform effect across all peptides (Fig. 4 *F* and *G* and *SI Appendix*, Fig. S4).

While the weak dissociation constants of these mutants limit power to detect bias changes, bias values calculated from the data displayed in Fig. 4 *F* and *G* and *SI Appendix*, Fig. S4 indicate that only mutation of H12$_{cc}$ in the PPARγ LBD-MRL24 complex affects bias. Independent testing of the effects of H4$_1$ mutations on bias indicate that H4$_1$ does not affect bias for the GW1929 complex and resulted in inconclusive results for the MRL24 complex (*SI Appendix*, Fig. S4).

Discussion

We define two classes of coactivator LxxLL helices, N-anchored and S motif based on bias values, sequence, and structural data. While corepressor CoRNR motif (31) vs. coactivator LxxLL motif binding mode is primarily differentiated by the helix length, N-anchored vs. S motif binding mode is differentiated by how and if the coactivator LxxLL helix bonds to helix 4. In addition, we found that helix capping can affect bias. We found that these structural differences allow two partial agonists and a full agonist to skew the PPARγ peptide binding profile toward S motif-containing peptides relative to rosiglitazone. Perhaps the most relevant previous work regarding the structural mechanisms of biased agonism came from Wu and coworkers. They reported that bonding to the helix 12 charge clamp, long considered essential for coactivator binding affinity, is less important for PPARγ coactivator 1α (PGC1α) binding to PPARγ or thyroid receptor TRβ1. They also found that the serine residue preceding the core LxxLL sequence in PGC1α contributed to the lack of helix 12 charge clamp dependence. They hypothesized that PGC1α has a different binding mode from other coactivators, mediated by the preceding serine and speculated that its unique binding mode could lead to coactivator bias and distinct pharmacology (47, 48). We have previously shown that inverse agonists of PPARγ induce distinct structural ensembles in the receptor and favor different corepressors (not coactivators), a kind of inverse agonist bias; however, our data did not reveal the underlying mechanism (27).

Our work used LxxLL (30) motif-containing peptides and not full-length coactivators; however, the binding mode differences we observe in peptides are expected to persist in the full-length coactivator and impact coactivator recruitment. While there is evidence that other coactivator regions interact with NRs (49, 50), LxxLL motifs are thought to largely control ligand-dependent binding to many NRs (16, 51, 52). In addition, while many coregulators have more than one such motif, the peptides we used either likely determine the binding of the whole coregulator to PPARγ (e.g., PGC1α$_{144}$, CBP$_{70}$, and

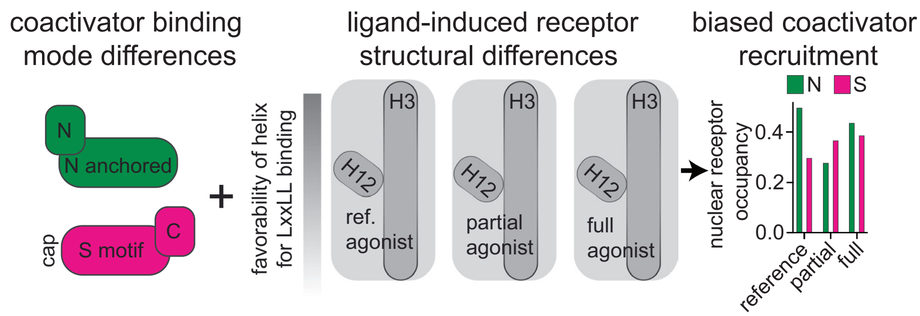

Fig. 5. Mechanisms of biased agonism in NRs. Coactivator binding mode differences are illustrated by the green and magenta shapes. The NR is shown as the large gray rectangle. The opacity of helices 3 and 12 indicate favorability of the Helix to LxxLL motif binding. Ligand-specific changes to receptor structure result in different occupancies of coactivators containing N-anchored and S motif LxxLL motifs at receptor-associated enhancers.

$NCOR_{2263}$; *SI Appendix*, Table S4) or have at least fourfold higher affinity for PPARγ than the other motifs we tested ($MED1_{645}$, $NCOA1_{1435}$, and $NRIP1_{501}$; *SI Appendix*, Table S5). Previously published reports using PPARγ and full-length coregulators or receptor interaction domains qualitatively support our finding that partial agonists skew binding toward PGC1α and away from CBP and MED1 relative to rosiglitazone (*SI Appendix*, Table S1). Together, these data support the hypothesis that certain non-TZD agonists and partial agonists cause biased coregulator recruitment relative to rosiglitazone in vivo. Examination of in vivo coregulator occupancy at enhancers and affinity-based bias measurements using full-length coregulators is needed to further test this hypothesis. Despite the need for further work, the structural and bias data presented here strongly support the hypothesis that some NR agonists are biased agonists relative to other agonists. A shift in our understanding of NR activation may be warranted, away from the notion that agonists simply potentiate coactivator vs. corepressor binding, toward a model that allows for agonist-specific coactivator binding profiles and physiologic effects.

Our data demonstrate how partial agonists induce bias relative to TZDs. Because partial agonists, including MRL24 and nTZDpa, activate the receptor without significant stabilization of helix 12, they bias coactivator recruitment away from N-anchored LxxLL peptides and toward S motifs. In contrast, rosiglitazone directly bonds with and strongly stabilizes helix 12 (17, 28, 53) and favors N-anchored peptides. Because bonding to $H4_8$ depends on $H12_{cc}$ and vice versa, a structurally unstable helix 12 disrupts both bonds, making N-anchored peptides very sensitive to the structural state of helix 12. Our data suggest that these differences in the coactivator binding mode and agonist-induced receptor structure underlie biased agonism of partial agonists relative to rosiglitazone. However, this mechanism cannot explain coactivator bias induced by GW1929, which, like rosiglitazone, is a full agonist and appears to stabilize helix 12 as much as rosiglitazone (28).

While we found that disruption of S/T capping and a bond just C-terminal to the $NRIP1_{501}$ helix affects GW1929-induced bias, additional work is necessary to fully understand the mechanisms by which GW1929 induces bias. One possible mechanism is ligand-specific changes to helix 3 structure. We previously found that the region of apo PPARγ helix 3 that contacts coregulator exchanges between two distinct conformations and that both nTZDpa and rosiglitazone dampen such exchange (27). Previously published HDX-MS data also suggest that nTZDpa, MRL24, and rosiglitazone stabilize helix 3 to similar degrees, while GW1929 may stabilize helix 3 better than these ligands (*SI Appendix*, Fig. S5). Because helix 3 stabilization may increase affinity for coactivators, superior helix 3 stabilization by GW1929 relative to rosiglitazone could underlie the coactivator bias observed for GW1929. While our $H3_{cc}$ mutation data do not support this notion, more work is needed to fully test this possibility. In addition, small ligand-specific differences in the shape and size, solvation, or conformational entropy state of the coregulator binding surface and entire receptor could contribute to coactivator bias (Fig. 5).

Ligand-specific coactivator binding profiles can produce agonist-specific physiologic differences because coactivators are not functionally interchangeable (33) and their effect on transcription can depend on what other factors are present at the enhancer DNA (6, 8). There is some evidence that increased NCOA1 and PGC1α recruitment and decreased recruitment of CBP and MED1 to PPARγ may be beneficial for metabolic syndrome and insulin sensitization (21, 33, 54). Interestingly, both NRIP1 and the long isoform of NCOA1 (which includes $NCOA1_{1435}$) can increase transcription from some enhancers/promoters but decrease transcription from others (38, 52, 55). Because NRIP1 primarily acts as a corepressor and has seven S motifs, our work suggests a mechanism by which NR partial agonists could favor retention of an LxxLL motif-containing corepressor (NRIP1).

We presented quantitative biochemical and structural evidence of biased NR agonism. These data suggest a physical mechanism that can explain how agonists favor the binding of certain LxxLL motifs and coactivators containing such motifs. Future work testing whether coactivator bias occurs in cells and connecting coactivator bias to physiologic effects in animals will help determine the extent to which undesired and desired effects of NR activation can be separated using ligand bias.

Methods

Protein Purification. Proteins were expressed in *E. coli* and purified as described previously (27). Briefly, n-terminally tagged 6xHis-TEV-PPARg LBD (PPARγ isoform 1/2 numbering: 202/230–477/505), 6xHis-PPARγ (isoform 2, 1-505), or 6xHis-TEV-RxRα was expressed in BL21-De3 Gold cells (Invitrogen) in either Luria-Bertani broth (PPARγ LBD) or terrific broth (PPARγ and RxRα full-length). Cells were grown at 37 °C to an OD of 0.8, dropped to 22 °C for 1 h, and then induced with 0.5 mM isopropyl β-D-1-thiogalactopyranoside (IPTG) for 16 h. Cells were harvested and lysed in 50 mM KPO4 (pH 8.0), 300 mM KCl, 1 mM TCEP, and 1 mM EDTA using a C-5 Emulsiflex high-pressure homogenizer (Avestin). Clarified lysate was flowed through two Histrap FF 5 mL columns in series (GE Healthcare). PPARγ LBD was incubated with 6xHis-tagged TEV overnight and passed through Histrap FF columns again to remove the 6xHis tag and TEV protease. Full-length protein was not cleaved with TEV. Size exclusion chromatography was then performed using a Hiload 16/600 Superdex 75 pg column (GE Healthcare), and purity was confirmed by SDS-page.

X-ray Crystallography and Structure Refinement. Purified PPARγ LBD was mixed with 1× molar MED1 peptide or 5× molar CBP peptide and then incubated at room temperature with 1:1 molar ratio GW1929 at 250 uM, in buffer 25 mM MOPS, 25 mM KCl, and 1 mM EDTA. The CBP complex was then buffer exchanged using a Millipore Centricon (Sigma) to remove excess peptide. Samples were concentrated to 10 mg/mL. Crystals were made by sitting-drop vapor diffusion in 2-well Intelli-plate 96 (Hampton Research) and formed overnight at 20°. Crystallization drops contained 0.3 μL of protein complex and 0.3 μL of reservoir solution containing 1 M sodium citrate tribasic dihydrate, 0.1 M sodium cacodylate, and pH 6.5 for the CBP complex or 100 mM HEPES 25% (w/v) PEG 2000 MME for the MED1 complex. Crystals were flash-frozen in liquid nitrogen, and data collection was carried out at SSRL Beamline 9-2 (SLAC National Accelerator Laboratory) for the CBP complex and APS BEAMLINE 19-BM (Advanced Proton Source) for the MED1 complex. Data integration and scaling was performed in HKL3000, and structures were solved by molecular replacement using the PHASER package in PHENIX on the previously published PPARγ structure 5TTO as a search model. The structure was further refined using PHENIX and Coot and deposited into the Protein Data Bank. This paper reports structures with PDB codes 7RLE and 6D94.

Direct Fluorescence Anisotropy. We performed fluorescence anisotropy assays by adding various concentrations of receptor–ligand complexes (1:1 molar ratio) or the receptor into wells containing 50 nM fluorescein-labeled peptide to generate 12-or-24 point curves of increasing receptor–ligand concentration. Experiments were performed in low-volume, 384-well, black plates (Grenier Bio-one, catalog number 784076), and the final volume in each well was 16 μL. Assay buffer contained 25 mM MOPS (pH 7.4), 25 mM KCl, 1 mM EDTA, 0.01% fatty-acid-free bovine serum albumin (BSA) (EMD Millipore, catalog number 126575), 0.01% Tween, and 5 mM TCEP. Plates were incubated at room temperature, away from light, for 2 h prior to reading on a Synergy H1 microplate reader (BioTek). Plates were read by excitation at 485 nm/20 nm of vertically polarized light, and emission at 528 nm/20 nm of vertically and horizontally polarized light was measured. Anisotropy was calculated using parallel and perpendicular light intensity using the following equation:

$$\text{Anisotropy} = \frac{I_{\parallel} - I_{\perp}}{I_{\parallel} + 2I_{\perp}}.$$

Anisotropy experiments with heterodimer were either performed by adding RxRα into an experimental plate with PPARγ at a 1:1 molar ratio, incubating for an additional 2 h, and then rereading in a plate reader (accounting for protein dilution in the final titration curve) or by forming the heterodimer by incubating PPARγ and RxRα together prior to titrating to a 12-or-24 point concentration curve. Anisotropy experiments with DNA used the SULT2A1 PPRE, (5′-GTAAAATAGGTGAAAGGTAA-3′), dsDNA, purchased from Integrated DNA Technologies. These experiments were similarly performed by either adding dsDNA with PPARγ and RxRα at a 1:1:1 concentration, incubating for an additional 2 h (6 h total), and then rereading in a plate reader or by incubating PPARγ, RxRα, and DNA together to form the complex prior to titration.

The K_d of RXRα LBD for the PPARγ LBD is less than 1 nM and that of DNA for the heterodimer is less than 10 nM (*SI Appendix*, Fig. S1), thus heterodimerization and DNA binding should be near complete around the much higher peptide–receptor K_d values. We also confirmed that we use sufficient incubation time to reach peptide and agonist binding equilibrium (56) (using the PPARγ LBD) (*SI Appendix*, Fig. S1).

We tried measuring the effect of the H67A mutation on CBP bias using direct anisotropy; however, the H67A dramatically decreased the affinity of CBP70 for PPARγ, making the highly bound state hard to achieve due to limiting solubility of PPARγ (*SI Appendix*, Fig. S4). To overcome these limitations, we instead used competitive anisotropy to measure the effect of the H67A mutation.

Competitive Peptide Fluorescence Anisotropy. Competitive fluorescence anisotropy assays were performed by preloading PPARγ LBD at 1.6 μM with equimolar FITC-Ahx-MED1$_{645}$ tracer peptide (synthesized by Lifetein, sequence: FITC-Ahx-NTKNHPMLMNLLKDNPAQD-NH2) and equimolar ligand. Acetylated PGC1α$_{144}$, CBP$_{70}$, or CBP$_{70}$ H67A peptides (Lifetein) were titrated using 24-point curves. All other assay parameters for competitive anisotropy are identical to the methods outlined above. Calculation of an inhibitory constant (K_i) value requires measurement of the affinity of the tracer peptide for each PPARγ–ligand complex. For the calculation of K_i values, we used the K_d value of the tracer peptide for each PPARγ–ligand complex measured on the same day with the same protein prep.

Anisotropy vs. acetylated peptide concentrations were graphed, and curves were fit in Prism using the "[Agonist] vs. response–variable slope" equation to determine IC_{50}. To calculate K_i, a modification of the Cheng–Prusoff equation devised by Huang et al. (57) and algebraically manipulated by Auld et al. (58) was used:

$$K_i = \frac{IC_{50}}{\frac{1}{1-F_0} + \frac{L_0(2-F_0)}{2K_d}} - K_d\left[\frac{F_0}{2-F_0}\right],$$

where F_0 is the fraction of tracer peptide bound and L_0 is the total tracer peptide concentration (1.6 μM). This equation is used because >10% of tracer is bound under the conditions we used. Fraction of tracer bound was estimated using a custom python 2.7 script (script available on the center for open science repository at osf.io/m98we). Script generated fraction-bound values were verified using a web-based tool available here: https://www.wolframalpha.com/widgets/view.jsp?id=3f9ea5a91e04b49316f83f8143fffa30

LanthaScreen Fluormone Ligand K_d Experiments. Fluormone pan-PPAR binding fluorescent ligand (5 nM; ThermoFisher), lab-purified 6xHis-PPARγ LBD (8 nM), and anti-His terbium (2.5 nM) were used to test ligand K_i for PPARγ. The LanthaScreen TR-FRET PPAR alpha Competitive Binding Assay Kit, goat (PV4892; ThermoFisher) was used to measure K_i of ligands for PPARα. We used kit-provided PPARα LBD GST (2 nM) and terbium-labeled anti-GST antibody (2.5 nM) along with Fluormone pan-PPAR ligand (5 nM). The LanthaScreen TR-FRET PPAR Delta Competitive Binding Assay Kit (PV4893; ThermoFisher) was used to measure K_i of ligands for PPARδ. We used kit-provided PPARδ LBD GST (8 nM) and terbium-labeled anti-GST antibody (2.5 nM) along with Fluormone pan-PPAR ligand (20 nM). All components of the assay (PPARα/δ/γ, test ligands, Fluormone, etc.) were diluted into 25 mM MOPS, 25 mM KCl, 1 mM EDTA, 5 mM TCEP, 0.01% Tween, and 0.01% low-lipid BSA to make the appropriate concentrations for adding to individual wells. Wells were excited at 340 nm and read at 495 nm and 520 nm. All concentrations listed above are the final concentration of the component at TR-FRET measurement. IC50 values were fit using GraphPad Prism nonlinear regression "[Inhibitor] vs. response–variable slope (four parameters)". K_i values were calculated using the Huang-derived equation above.

TR-FRET. TR-FRET was used to measure the dissociation constant of PPARγ for RXRα in *SI Appendix*, Fig. S1. One molar equivalent of ligands (or equivalent volume of DMSO vehicle) was added to labeled PPARγ LBD (Q373C-HiLyte 488 C313A). PPARγ was then titrated into 500 pM 6xHis-RXRα LBD/Anti 6HIS-Tb cryptate, RXRα agonist (50 nM 9-cis retinoic acid), and 1 μM additional matching ligand (or equivalent volume of vehicle).

PPRE Assay. HEK293T cells were cultured for two passages post thaw. They were plated at a density of 3.82 × 10^6 cells in a T75 flask and then transfected using XtremeGene 9 (Millipore Sigma) with a luciferase reporter plasmid containing three PPAR response elements (PPREs) and a full-length PPARγ isoform 2 expressing plasmid (gifts from the Douglas Kojetin lab). Every μg of plasmid DNA was complexed with 3 μL of XtremeGene 9 in accordance with XtremeGene 9 protocols. Then, 8.6 μg of DNA was used on each plate. Equal masses of each plasmid were added. The plasmids were a gift from Douglas Kojetin (Scripps Research). The cells were incubated in the transfection medium overnight. The cells were removed from the plate by pipetting and plated into white 384 well plates at 10,000 cells/well in 20 μL medium per well. After 4 h, 20 μL of medium with drug was added to each well for the final concentration of 28 nM GW1929, 2.5 μM GW1929, 361 nM rosiglitazone, 2.5 μM rosiglitazone, 68 nM T0070907, or 2.5 μM T0070907. Blocking experiments were treated with 68 nM T0070907 3 h prior to drug treatment. The cells were incubated overnight. After incubation, 20 mL of BriteLite Plus from PerkinElmer was added, and the plates were read on a plate reader.

PPARγ LBD Delipidation. PPARγ LBD was delipidated using Lipidex 1,000 resin. PPARγ LBD at 0.8 mg/mL was batched with resin at equal volume for 45 min, shaking at 100 rpm, at 37 °C. After batching, protein was quickly eluted off resin using syringe force in a tabletop Econo-column (Life Science Research). Resin was washed with one column volume of warm delipidation buffer (25 mM MOPS pH 7.4, 25 mM KCl, and 1 mM EDTA), and wash was pooled into elution prior to concentration of protein with Millipore Centricon concentrators (Sigma). Protein in this work that is not delipidated is designated as containing *E. coli* lipids as these have been shown to copurify with PPARγ from *E. coli* (26). Full-length PPARγ and RXRα and RXRα LBD were not delipidated.

Ligands. The source and product number of ligands utilized here are listed in *SI Appendix*, Table S7.

Peptides. Most peptides used in anisotropy experiments were 5-FAM labeled, however, a few peptides were labeled with FITC. FITC was usually connected via a 6-aminohexanoic acid (Ahx) 6 carbon linker to the peptide. The exact sequence, labeling, and terminal modification (if any) of all the peptides used here are listed in *SI Appendix*, Table S8.

Curve Fitting. We fit dissociation constants of coregulator peptides for receptors using GraphPad Prism 9 using the same equation we used previously (18):

$$A_{obs} = (A_b - A_f)\ \frac{K_d + L_{st} + R_t - \sqrt{(K_d + L_{st} + R_t)^2 - 4L_{st}R_t}}{2L_{st}} + A_f,$$

where A_{obs} is the measured anisotropy, A_b and A_f are the anisotropy values of the peptide bound to the receptor and free in solution respectively, K_d is the dissociation constant, and L_{st} and R_t are the total concentrations of the fluorescently labeled peptide and the receptor, respectively. When the bottom (A_f) or top (A_b) were not well defined, they were constrained to be a shared value across replicates. The Dataset S1 notes such fitting details.

Mutational Analysis. Mutations in PPARγ LBD were made using the QuikChange Lightning Site-Directed Mutagenesis kit (Agilent) using primers listed previously (27). Mutations were confirmed by Sanger sequencing (Eurofins). ΔG_{app} was calculated (59) by comparing WT to mutant PPARγ LBD/peptide affinities for coregulators. The free energy of binding is related to the dissociation constant for the peptide receptor pair by the following relationship:

$$\Delta G = RTln(K_d)\ ,$$

where R and T are the ideal gas constant and temperature, respectively. The change in binding energy due to mutation of the receptor can be attained using a related calculation (59).

$$\Delta G_{bind} = RTln(\frac{K_{d\ wt}}{K_{d\ mutant}}).$$

Assuming that the receptor mutation does not disturb the receptor structural state, then the overall change in binding energy should indicate the energetic contribution of the disrupted protein–peptide bond (59). The change in binding energy from $H12_{cc}$, $H3_{cc}$, and $H4_1$ mutations likely arises from disruption of coactivator–PPARγ bonding and not disruption of the native PPARγ structure. Structures and simulations indicate that $H12_{cc}$, $H3_{cc}$, and $H4_1$ can bond to partner receptor residues on the same helix; however, simulations indicate that these residues mainly interact with the solvent (*SI Appendix*, Fig. S4). In addition, mutation of the residue that forms the most frequent intrahelical bond with $H12_{cc}$ (K474) does not significantly affect PPARγ affinity for coregulators (28). Because $H4_8$ hydrogen bonds to helix 12, in addition to N-anchored coactivators (Fig. 3*A*), its mutation can disrupt the receptor structure (27). For this reason, we chose to mutate the coactivator (CBP_{70} H67A) instead of the receptor.

Bias Calculation. See Fig. 1*F* for the method used to calculate bias. We calculate and display the variance for the reference peptide (CBP) by subtracting individual replicate CBP sigma (σ) values from each other to best match the method used for nonreference peptide calculations. For convenience, we subtracted adjacent replicates in the excel file as shown below for n replicates (Dataset S1):

$$\frac{\sigma_1 - \sigma_2}{\sqrt{2}} \cdots \frac{\sigma_{n-1} - \sigma_n}{\sqrt{2}}, \frac{\sigma_n - \sigma_1}{\sqrt{2}}.$$

Several lines of evidence indicate that bias values are driven by peptide affinity for PPARγ and not RXRα. First, PPARγ and heterodimer bias values are similar. Second, the peptides we use have at least a sixfold higher affinity for PPARγ LBD than RXRα LBD. Finally, heterodimers containing mutated PPARγ (E471L) that does not bind coactivator peptides well have much lower affinity for almost all the peptides compared to WT heterodimer; the two exceptions, $NRIP1_{501}$ and $NCOR1_{2263}$, have high affinity for the PPARγ mutant, not RXRα (*SI Appendix*, Fig. S1).

Statistical Analysis. We identified three potential sources of variance in our anisotropy experiments: 1) differences between the receptor purification batches, 2) pipetting error while performing serial dilutions of the stock receptor (or peptide for competitive fluorescence anisotropy), and 3) pipetting error while performing all other steps in the assay. Because we add ligand to the receptor and then perform a serial dilution of the receptor–ligand complex in buffer, sources 2 and 3 are present for all experiments comparing coregulator peptide affinities for receptor bound to different ligands (or between apo and ligand-bound receptor). To capture the variance produced by such unavoidable pipetting errors, we performed replicates using independent serial dilutions of the receptor from the same purification batch (with or without added ligand). Source number 1 of error is unavoidable when making comparisons between mutant receptors and WT receptor. To account for this source of variance, we performed replicates using PPARγ from different purification batches. We also used such purification batch replicates at times when making other comparisons. Such details are noted in the figure legends and in the Dataset S1.

Structural Analysis. We used Chimera (60) to determine hydrogen bonding using default settings, except in Fig. 3*A* where the default h-bonding length constraint was relaxed by 0.2 Angstroms for the PGC1α panel to allow display of the S/T capping bond. For complete analysis data, including exact structures analyzed, see the file structural analysis.xlsx, which is available on the center for open science repository at https://osf.io/m98we/.

Simulations. In silico simulations were started from PDB 2PRG chain A (12). Missing residues were modeled using the Modeller program in Chimera (61). The likely protonation states were assigned by H^{++} at pH 7.4 and 50 mM salt concentration (http://biophysics.cs.vt.edu/H++) (62). The residue names were then converted to Amber names using pdb4amber (63). We used the R.E.D. Server to derive point charges for the ligand (64). A forcefield is created from the ligand using Antechamber, GAFF2 atoms (63), and the parmchk2 tool (63). Tleap was then used to create the complete in silico system using the ff14SB forcefield and TIP3p waters in a truncated octahedron periodic box (63,65,66). In addition to water, Tleap was used to add Na^+ Cl^- ions to neutralize the system and to add KCl to make a K^+ concentration of 50 mM (67).

The system is minimized via a nine-step minimization as described previously (27). We used the Amber ParMed tool for hydrogen mass repartitioning (63) to allow 4 fs steps. Production runs used GPU-enabled Amber 16 [pmemd.cuda (63)] at 310 K with coordinates saved at 100 ps intervals.

CPPTRAJ is used to find hydrogen bonds and solvent interactions (68). The simulation was analyzed every 100 saved frames (10 ns). The hydrogen bond files were then grouped into backbone and sidechains by residue using the hbond_scatter_mult2.py script.

Data, Materials, and Software Availability. All data generated or analyzed during this study are included in this published article (and its SI Appendix files) with the exception of the raw molecular dynamics simulation data and compiled data from analysis of all NR structures. The structural analysis data can be found on the center for open science repository at https://osf.io/m98we/ (69). The raw simulation data are large but are available from the corresponding author on reasonable request.

ACKNOWLEDGMENTS. We thank Dr. Stephen Sprang and Tung-Chung Mou and the integrated structural biology core for assistance in X-ray crystallography. Computational resources and support from the University of Montana's Griz Shared Computing Cluster (GSCC) and the University of Montana molecular computation core facility (MCCF) contributed to this research. This work was supported by NIH grants R00DK103116 and R01DK129646 (T.S.H.) and a subproject award to T.S.H. from COBRE grant 5P20GM103546 (PI: Stephen Sprang). Additional funding for this work was provided by the vice president for research and creative scholarship at the University of Montana.

Author affiliations: [a]Center for Biomolecular Structure and Dynamics, University of Montana, Missoula 59812; [b]Biochemistry and Biophysics Graduate program, University of Montana, Missoula 59812; and [c]Department of Biomedical and Pharmaceutical Sciences, University of Montana, Missoula 59812

1. R. Santos *et al.*, A comprehensive map of molecular drug targets. *Nat. Rev. Drug Discov.* **16**, 19–34 (2017).
2. S. E. Kahn *et al.*, Glycemic durability of rosiglitazone, metformin, or glyburide monotherapy. *N. Engl. J. Med.* **355**, 2427–2443 (2006).
3. R. E. Soccio, E. R. Chen, M. A. Lazar, Thiazolidinediones and the promise of insulin sensitization in type 2 diabetes. *Cell Metab.* **20**, 573–591 (2014).
4. T. P. Burris *et al.*, Nuclear receptors and their selective pharmacologic modulators. *Pharmacol. Rev.* **65**, 710–778 (2013).
5. N. E. Bruno *et al.*, Chemical systems biology reveals mechanisms of glucocorticoid receptor signaling. *Nat. Chem. Biol.* **17**, 307–316 (2021).
6. G. Stampfel *et al.*, Transcriptional regulators form diverse groups with context-dependent regulatory functions. *Nature* **528**, 147–151 (2015).
7. F. Reiter, S. Wienerroither, A. Stark, Combinatorial function of transcription factors and cofactors. *Curr. Opin. Genet. Dev.* **43**, 73–81 (2017).
8. S. R. Grossman *et al.*, Systematic dissection of genomic features determining transcription factor binding and enhancer function. *Proc. Natl. Acad. Sci. U.S.A.* **114**, E1291–E1300 (2017).
9. M. Ahmadian *et al.*, PPARgamma signaling and metabolism: The good, the bad and the future. *Nat. Med.* **19**, 557–566 (2013).
10. P. Li *et al.*, Adipocyte NCoR knockout decreases PPARγ phosphorylation and enhances PPARγ activity and insulin sensitivity. *Cell* **147**, 815–26 (2011).
11. J. Jumper *et al.*, Highly accurate protein structure prediction with AlphaFold. *Nature* **596**, 583–589 (2021).
12. R. T. Nolte *et al.*, Ligand binding and co-activator assembly of the peroxisome proliferator-activated receptor-γ. *Nature* **395**, 137–143 (1998).
13. I. M. S. de Vera *et al.*, Synergistic regulation of coregulator/nuclear receptor interaction by ligand and DNA. *Structure* **25**, 1506–1518.e4 (2017).
14. Y. Li, A. Kovach, K. Suino-Powell, D. Martynowski, H. E. Xu, Structural and biochemical basis for the binding selectivity of peroxisome proliferator-activated receptor gamma to PGC-1alpha. *J. Biol. Chem.* **283**, 19132–19139 (2008).
15. E. M. McInerney *et al.*, Determinants of coactivator LXXLL motif specificity in nuclear receptor transcriptional activation. *Genes Dev.* **12**, 3357–3368 (1998).
16. D. M. Heery, S. Hoare, S. Hussain, M. G. Parker, H. Sheppard, Core L XX LL motif sequences in CREB-binding protein, SRC1, and RIP140 define affinity and selectivity for steroid and retinoid receptors. *J. Biol. Chem.* **276**, 6695–6702 (2001).
17. J. B. Bruning *et al.*, Partial agonists activate PPARgamma using a helix 12 independent mechanism. *Structure* **15**, 1258–1271 (2007).
18. J. Shang *et al.*, A molecular switch regulating transcriptional repression and activation of PPARγ. *Nat. Commun.* **11**, 956 (2020).
19. J. H. Choi *et al.*, Antidiabetic actions of a non-agonist PPARγ ligand blocking Cdk5-mediated phosphorylation. *Nature* **477**, 477–481 (2011).
20. C. R. Bartman *et al.*, Transcriptional burst initiation and polymerase pause release are key control points of transcriptional regulation. *Mol. Cell* **73**, 519–532.e4 (2019).
21. A. Boija *et al.*, CBP regulates recruitment and release of promoter-proximal RNA polymerase II. *Mol. Cell* **68**, 491–503.e5 (2017).
22. J. Soutourina, Transcription regulation by the mediator complex. *Nat. Rev. Mol. Cell Biol.* **19**, 262–274 (2018).
23. L. El Khattabi *et al.*, A pliable mediator acts as a functional rather than an architectural bridge between promoters and enhancers. *Cell* **178**, 1145–1158.e20 (2019).
24. J. J. Acton *et al.*, Benzoyl 2-methyl indoles as selective PPARγ modulators. *Bioorg. Med. Chem. Lett.* **15**, 357–362 (2005).
25. J. P. Berger *et al.*, Distinct properties and advantages of a novel peroxisome proliferator-activated protein [gamma] selective modulator. *Mol. Endocrinol.* **17**, 662–676 (2003).
26. M. V. Liberato *et al.*, Medium chain fatty acids are selective peroxisome proliferator activated receptor (PPAR) γ activators and pan-PPAR partial agonists. *PLoS One* **7**, e36297 (2012).
27. Z. Heidari *et al.*, Definition of functionally and structurally distinct repressive states in the nuclear receptor PPARγ. *Nat. Commun.* **10**, 5825 (2019).
28. I. M. Chrisman *et al.*, Defining a conformational ensemble that directs activation of PPARγ. *Nat. Commun.* **9**, 1794 (2018).
29. J. Shang *et al.*, Cooperative cobinding of synthetic and natural ligands to the nuclear receptor PPARγ. *Elife* **7**, 11–15 (2018).
30. B. D. Darimont *et al.*, Structure and specificity of nuclear receptor—coactivator interactions. *Genes Dev.* **12**, 3343–3356 (1998).
31. C. A. Phelan *et al.*, Structure of rev-erbα bound to N-CoR reveals a unique mechanism of nuclear receptor–co-repressor interaction. *Nat. Struct. Mol. Biol.* **17**, 808–814 (2010).
32. K. A. Temple *et al.*, An intact DNA-binding domain is not required for peroxisome proliferator-activated receptor gamma (PPARgamma) binding and activation on some PPAR response elements. *J. Biol. Chem.* **280**, 3529–3540 (2005).
33. L. Mouchiroud, L. J. Eichner, R. J. Shaw, J. Auwerx, Transcriptional coregulators: Fine-tuning metabolism. *Cell Metab.* **20**, 26–40 (2014).
34. J. H. Choi *et al.*, Anti-diabetic drugs inhibit obesity-linked phosphorylation of PPARγ by Cdk5. *Nature* **466**, 451–456 (2010).
35. B. R. Henke *et al.*, N -(2-benzoylphenyl)- l -tyrosine PPARγ agonists. 1. Discovery of a novel series of potent antihyperglycemic and antihyperlipidemic agents. *J. Med. Chem.* **41**, 5020–5036 (1998).
36. P. Kolb *et al.*, Community guidelines for GPCR ligand bias: IUPHAR review 32. *Br. J. Pharmacol.* **179**, 3651–3674 (2022).
37. S. Rajagopal *et al.*, Quantifying ligand bias at seven-transmembrane receptors. *Mol. Pharmacol.* **80**, 367–377 (2011).
38. J. Nautiyal, Transcriptional coregulator RIP140: An essential regulator of physiology. *J. Mol. Endocrinol.* **58**, R147–R158 (2017).
39. A. Mottis, L. Mouchiroud, J. Auwerx, Emerging roles of the corepressors NCoR1 and SMRT in homeostasis. *Genes Dev.* **27**, 819–835 (2013).
40. G. Lee *et al.*, T0070907, a selective ligand for peroxisome proliferator-activated receptor ??, functions as an antagonist of biochemical and cellular activities. *J. Biol. Chem.* **277**, 19649–19657 (2002).
41. M. F. Broekema *et al.*, Natural helix 9 mutants of PPARγ differently affect its transcriptional activity. *Mol. Metab.* **20**, 115–127 (2019).
42. C. Y. Chang *et al.*, Dissection of the LXXLL nuclear receptor-coactivator interaction motif using combinatorial peptide libraries: Discovery of peptide antagonists of estrogen receptors α and β. *Mol. Cell. Biol.* **19**, 8226–8239 (1999).
43. E. Hur *et al.*, Recognition and accommodation at the androgen receptor coactivator binding interface. *PLoS Biol.* **2**, E274 (2004).
44. F. R. Santori *et al.*, Identification of natural RORγ ligands that regulate the development of lymphoid cells. *Cell Metab.* **21**, 286–298 (2015).
45. N. E. Newell, Mapping side chain interactions at protein helix termini. *BMC Bioinformatics* **16**, 1–21 (2015).
46. R. Aurora, G. D. Rose, Helix capping. *Protein Sci.* **7**, 21–38 (1998).
47. Y. Wu, W. W. Chin, Y. Wang, T. P. Burris, Ligand and coactivator identity determines the requirement of the charge clamp for coactivation of the peroxisome proliferator-activated receptor γ. *J. Biol. Chem.* **278**, 8637–8644 (2003).
48. Y. Wu, P. Delerive, W. W. Chin, T. P. Burris, Requirement of helix 1 and the AF-2 domain of the thyroid hormone receptor for coactivation by PGC-1. *J. Biol. Chem.* **277**, 8898–8905 (2002).
49. X. Yu *et al.*, Structural insights of transcriptionally active, full-length androgen receptor coactivator complexes. *Mol. Cell* **79**, 812–823.e4 (2020).
50. A. Y. Belorusova *et al.*, Molecular determinants of MED1 interaction with the DNA bound VDR–RXR heterodimer. *Nucleic Acids Res.* **48**, 11199–11213 (2020).
51. D. M. Heery, E. Kalkhoven, S. Hoare, M. G. Parker, A signature motif in transcriptional co-activators mediates binding to nuclear receptors. *Nature* **387**, 733–736 (1997).
52. E. Kalkhoven, J. E. Valentine, D. M. Heery, M. G. Parker, Isoforms of steroid receptor co-activator 1 differ in their ability to potentiate transcription by the oestrogen receptor. *EMBO J.* **17**, 232–243 (1998).
53. T. S. Hughes *et al.*, Ligand and receptor dynamics contribute to the mechanism of graded PPARγ agonism. *Structure* **20**, 139–150 (2012).
54. T. Yamauchi *et al.*, Increased insulin sensitivity despite lipodystrophy in Crebbp heterozygous mice. *Nat. Genet.* **30**, 221–226 (2002).
55. O. C. Meijer *et al.*, Steroid receptor coactivator-1 splice variants differentially affect corticosteroid receptor signaling. *Endocrinology* **146**, 1438–1448 (2005).
56. I. Jarmoskaite, I. Alsadhan, P. P. Vaidyanathan, D. Herschlag, How to measure and evaluate binding affinities. *Elife* **9**, 1–34 (2020).
57. X. Huang, Fluorescence polarization competition assay: The range of resolvable inhibitor potency is limited by the affinity of the fluorescent ligand. *J. Biomol. Screen.* **8**, 34–38 (2003).
58. D. S. Auld *et al.*, "Receptor binding assays for HTS and drug discovery" in *Assay Guidance Manual* (Eli Lilly & Company and the National Center for Advancing Translational Sciences, Bethesda, 2004), pp. 1–42.
59. A. R. Fersht, Relationships between apparent binding energies measured in site-directed mutagenesis experiments and energetics of binding and catalysis. *Biochemistry* **27**, 1577–1580 (1988).
60. V. Chandra *et al.*, Structure of the intact PPAR-γ–RXR-α nuclear receptor complex on DNA. *Nature* **456**, 350–356 (2008).
61. A. Šali, T. L. Blundell, Comparative protein modelling by satisfaction of spatial restraints. *J. Mol. Biol.* **234**, 779–815 (1993).
62. R. Anandakrishnan, B. Aguilar, A. V. Onufriev, H++ 3.0: Automating pK prediction and the preparation of biomolecular structures for atomistic molecular modeling and simulations. *Nucleic Acids Res.* **40**, 537–541 (2012).
63. D. A. Case *et al.*, *AMBER 2016 Reference Manual* (2016). AMBER version used: Amber16 and AmberTools16. University of California, San Francisco, San Francisco, California 94143
64. E. Vanquelef *et al.*, Server: A web service for deriving RESP and ESP charges and building force field libraries for new molecules and molecular fragments. *Nucleic Acids Res.* **39**, 511–517 (2011).
65. J. A. Maier *et al.*, ff14SB: Improving the accuracy of protein side chain and backbone parameters from ff99SB. *J. Chem. Theory Comput.* **11**, 3696–3713 (2015).
66. D. Vassetti, M. Pagliai, P. Procacci, Assessment of GAFF2 and OPLS-AA general force fields in combination with the water models TIP3P, SPCE, and OPC3 for the solvation free energy of druglike organic molecules. *J. Chem. Theory Comput.* **15**, 1983–1995 (2019).
67. S. Joung, T. E. Cheatham, Molecular dynamics simulations of the dynamic and energetic properties of alkali and halide ions using water-model-specific ion parameters. *J. Phys. Chem. B* **113**, 13279–13290 (2009).
68. D. R. Roe, T. E. Cheatham III, T. E. Cheatham, PTRAJ and CPPTRAJ: Software for processing and analysis of molecular synamics trajectory data. *J. Chem. Theory Com.* **9**, 3084–3095 (2013).
69. T. S. Hughes, A structural mechanism of nuclear receptor biased agonism, Open Science Framework database, https://osf.io/m98we/, deposited May 28 2022.